

THE ATMOSPHERE OF NEPTUNE: AN ANALYSIS OF RADIO OCCULTATION DATA ACQUIRED WITH VOYAGER 2

GUNNAR F. LINDAL

Jet Propulsion Laboratory, California Institute of Technology, Pasadena, California 91109

Received 22 August 1991; revised 19 November 1991

ABSTRACT

Recordings of the tracking signals received from Voyager 2 during its occultation by Neptune have been used to study the vertical structure of Neptune's atmosphere. The measurements, which began at a planetographic latitude of 62° north and ended near 45° south, cover an altitude interval of about 5000 km. Inversion and interpretation of the occultation data have provided new information on the distribution of free electrons in Neptune's ionosphere, the thermal structure and composition of its troposphere and stratosphere, and the zonal winds below the 1.7 bar level in the troposphere. The 1 bar isobaric surface has equatorial and polar radii of $24\,766 \pm 15$ km and $24\,342 \pm 30$ km, respectively, and a corresponding oblateness of 0.0171 ± 0.0014 . At this pressure level, the temperature was 72 ± 2 K. The tropopause was detected approximately 40 km above the 1 bar level at a pressure of about 100 mbar. A comparison with infrared observations indicates that the gas at the tropopause consists of 78%–84% hydrogen by number density with the rest being mostly helium. The temperature in this region was 52 ± 2 K. Above the tropopause, the temperature is increasing with altitude reaching 130 ± 12 K near the 0.3 mbar level. A 2–3 km thick layer with a small refractivity scale height whose top was detected 14 km below the 1 bar level, may be a region where the CH_4 mixing ratio is decreasing rapidly with increasing altitude—perhaps as a result of vapor condensation effects that produce haze. For the nominal model derived from the ingress measurements, this interpretation yielded a CH_4 mixing ratio of 2% at the base of the layer where the pressure was about 1.9 bars. Uncertainties in the atmospheric rotation period affect the interpretation of the measurements below the 1.7 bar level. A rotation period of 14.2 ± 0.3 hr was found to be consistent with the ingress data acquired at 60° north latitude, and was adopted for the nominal model. This rotation period corresponds to an eastward zonal wind velocity of 176 ± 32 m/s relative to the magnetic field. Data acquired between 38° and 15° south during egress indicate westward zonal winds with velocities ranging from 100 to 400 m/s below the 1.7 bar level. Ammonia vapor was assumed to be the principal microwave absorber limiting the depth of the measurements in the troposphere. At the lowest level where the link was detected during ingress, the nominal model has a pressure and temperature of 6.3 bars and 135 K, respectively. The ammonia mixing ratio at this level was 500 ± 150 parts per billion.

1. INTRODUCTION

In August of 1989, the Voyager 2 spacecraft passed through the Neptune system and was occulted by both the planet and its satellite Triton (Stone & Miner 1989). These events were observed at radio tracking stations in Australia and Japan (Tyler *et al.* 1989). Figure 1 shows the geometry of the spacecraft's occultation by Neptune.

During ingress, the radio link began probing Neptune's stratosphere near 62° north latitude and 227° east longitude where the first nondispersive effects of refraction were detected. The ingress measurements ended when the signals were absorbed in the troposphere at about 59° north and 205° east. Egress data were acquired in a region extending from about 15° south and 151° east, where the signals reappeared, to a location near 45° south and 131° east where the link periapsis emerged from the top of the detectable portion of the stratosphere. The longitude system used here is based on the 16.11 hr rotation period of the magnetic field (Warwick *et al.* 1989; Stone & Miner 1989), and the reference meridian was chosen so that the spacecraft was at 200° east longitude at the time of closest approach.

Voyager 2 transmitted two unmodulated and coherently related tracking carrier frequencies during the occultation measurements, one at X band (8.4 GHz) and the other at S band (2.3 GHz). Both frequencies were derived from a stable crystal oscillator placed in a temperature controlled oven

in the spacecraft. Transmission to the Earth was performed with a parabolic dish that was rigidly mounted on the spacecraft. The radiated power was approximately 19 W at X band and 7 W at S band, and both signals were right-hand circularly polarized. The diameter of the dish was 3.66 m, and the half-power beamwidths were approximately 0.6° and 2.4° at X and S band, respectively. In order to keep the refracted radio beams pointed at the receiving stations during the atmospheric measurements, the spacecraft was turned so that the antenna boresight tracked the virtual image of the Earth on the limb of Neptune.

During Voyager 2's flight past Neptune, the two spacecraft signals were received with a 70-m-diam parabolic dish at NASA's Deep Space Station (DSS) 43 at Tidbinbilla in Australia. Tracking instrumentation included both wideband and phase-locked-loop receiver channels with digitized outputs. The wideband recordings, which are usually considered the primary data set for atmospheric studies, consist of digital S- and X-band voltage samples taken at a rate of 50 000 per second. The phase-locked-loop recordings contain samples of the amplitude and frequency of the signal mode tracked by each receiver loop.

In addition to the data acquired at the NASA facility, the X-band signal from Voyager 2 was received with the 64 m Commonwealth Scientific and Industrial Research Organization (CSIRO) antenna at Parkes in Australia, and the S-band signal was received with the 64 m Institute of Space and

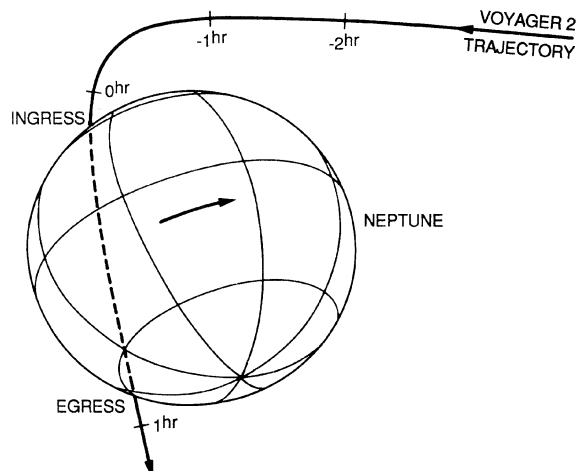


FIG. 1. View from the Earth of Voyager 2's occultation by Neptune. Time is marked along the spacecraft trajectory in hours past periapsis passage, which occurred at 3:55:40 UTC on 25 August 1989 when the spacecraft was 29 240 km from Neptune's center of mass. The occultation began at a planetographic latitude of 62° north and ended at 45° south. Both ingress and egress occurred near the morning terminator.

Astronautical Science (ISAS) antenna at Usuda in Japan. More information about the radio tracking instrumentation is available in previous publications (Eshleman *et al.* 1977; Edelson *et al.* 1979; Ham *et al.* 1989; Tyler *et al.* 1989; Kur-sinski & Asmar 1991).

Two earlier papers presented preliminary results on Nep-

tune's atmosphere based on studies of data acquired with both the phase-locked-loop and the wideband receiver channels (Tyler *et al.* 1989; Lindal *et al.* 1990). The purpose of this report is to provide a more complete summary of the analysis and interpretation of these occultation measurements.

2. DATA ANALYSIS AND RESULTS

The wideband recordings constitute the primary dataset for atmospheric studies because they provide the highest signal-to-noise ratios and allow detection of many signal modes appearing simultaneously at different frequencies during periods of multipath propagation. Reduction of the wideband data involved filtering, mixing, and decimation followed by signal detection to determine the amplitude and frequency of the various propagation modes. The results are summarized in Fig. 2, which shows the signal intensity and Doppler frequency perturbations observed while the tracking link was being refracted in Neptune's atmosphere.

As illustrated in the upper panels in Fig. 2, the spacecraft signals were affected by defocusing, scintillations, and absorption in the atmosphere of Neptune. For instance, the drop in the signal power recorded at approximately 8:08 UT during ingress was produced by defocusing as the tracking link moved down below the 10 mbar level in the stratosphere. Another abrupt power drop at 8:10 UT was caused by defocusing as the ray periapsis entered a 2–3 km thick layer with a small refractivity scale height located at the 1.9 bar level. This layer, which also produced multipath propagation and spectral frequency broadening, may be a region where the methane mixing ratio is decreasing with increasing altitude due to condensation effects that produce haze

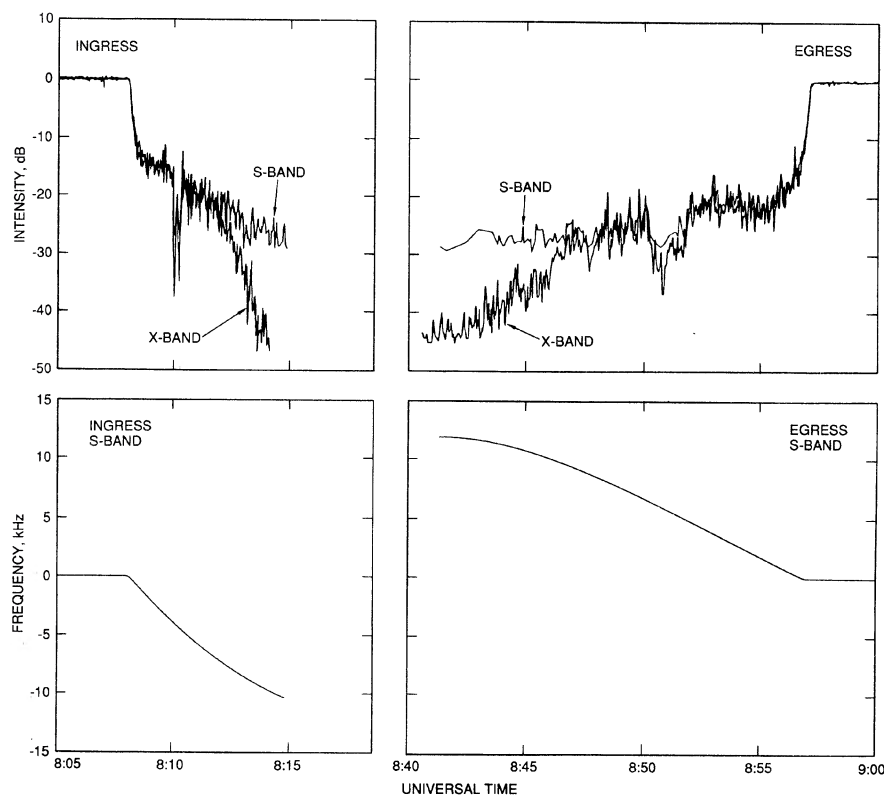


FIG. 2. Doppler frequency and signal intensity perturbations observed at Deep Space Station 43 during Voyager 2's occultation by Neptune. The measurements were conducted at wavelengths of 3.6 cm (X band) and 13 cm (S band), on 25 August 1989. Time of signal reception is marked in hours past midnight. It took the signals 4 hr and 6 min to travel from the spacecraft to the Earth.

(Tyler *et al.* 1989; Lindal *et al.* 1990). A similar layer was also detected during occultation measurements of the atmosphere of Uranus (Tyler *et al.* 1986; Eshleman *et al.* 1987; Lindal *et al.* 1987). When the radio link moved down below the 3 bar level, the signals were slowly extinguished by absorption. This effect is particularly striking at *X* band which has the highest signal-to-noise ratio. Similar intensity perturbations were observed during egress.

Neither H_2 , He, CH_4 , nor water vapor appear to have contributed appreciably to the observed signal attenuation. However, ammonia vapor, which has many strong absorption lines in the cm and mm wavelength region (Townes & Schawlow 1955; Berge & Gulkis 1976; Poynter & Pickett 1981; Spilker 1990; Joiner & Steffes 1991), can account for the observed signal loss and has previously been invoked to help explain the microwave brightness spectrum of Neptune (de Pater & Richmond 1989; Romani *et al.* 1989).

As in previous occultation experiments, the Doppler frequency and signal intensity perturbations recorded during ingress and egress have been used to study the vertical structure of the two atmospheric regions probed by the link. This was done by inverting the integral equations relating the vertical refractive index and microwave absorption profiles of the atmosphere to the observed frequency and intensity perturbations.

The basic problem of inverting radio occultation data acquired in a spherical atmosphere has been described in previous articles which provide both numerical and analytical transform solutions (Fjeldbo & Eshleman 1968; Fjeldbo *et al.* 1971; Eshleman 1973). Subsequent studies extend the technique to oblate planets where horizontal variations in pressure, temperature, and composition are negligible and the direction of the local vertical is defined by the external gravity field and the zonal wind velocities (Lindal *et al.* 1985).

The approach employed in the calculation of the refractive index profiles is based on geometrical optics and the concept that each frequency value recorded at the tracking station corresponds to a ray, or photon trajectory, which at its lowest point in the atmosphere tangentially grazes a geoid, i.e., a surface which is everywhere orthogonal to the local vertical. By starting with a ray grazing the top of the atmosphere and proceeding downward to lower and lower rays, one can compute the refractive index at the ray periaapses in a sequential manner so that each photon arrives at the tracking station with a frequency that matches the recorded frequency sample. A procedure for inverting radio occultation data is outlined in the Appendix.

Data acquired while the tracking link probed the stratosphere and troposphere during ingress cover a latitude range of about 3° . These measurements, which appear to be essentially unaffected by large-scale horizontal refractive index gradients and zonal wind shear, can be inverted by simply using a constant value for the rotation period. The egress measurements are more difficult to interpret, however, because they were obtained over a latitude range of about 30° , and seem to have been influenced by either variations in the rotation period or significant horizontal gradients. In what follows, we will first describe how the ingress measurements have been used to develop a nominal model for Neptune's atmosphere. Later, we will discuss alternative interpretations of the ingress data as well as the analysis of the egress data.

Figure 3 shows the nominal refractivity profile for Nep-

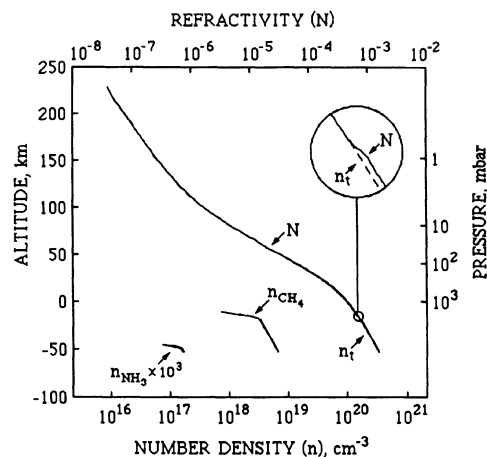


FIG. 3. Nominal gas refractivity (N) and number density profiles for Neptune's troposphere and stratosphere. The profiles were obtained by inverting the ingress data with an atmospheric rotation period of 14.2 hr. The total number density (n_i) was determined from the refractivity by adopting a helium to hydrogen abundance ratio of 19/81. As discussed in the text, the methane distribution was calculated by assuming that the layer with the small refractivity scale height shown in an expanded view in the upper right-hand corner of the figure, is a region where the methane mixing ratio is increasing rapidly with decreasing altitude. The ammonia distribution was inferred from the microwave absorption. Zero altitude corresponds to the 1 bar (or 10 N/cm^2) pressure level.

tune's troposphere and stratosphere. It was obtained from the ingress Doppler data acquired near 60° north latitude. The process leading to this profile was started by first using the frequency measurements at *S* band to correct the *X*-band data for dispersive effects caused by ionization along the tracking link. Next, the corrected *X*-band frequency measurements were inverted to obtain the refractivity (N) of the atmosphere, which is defined here as the refractive index reduced by one. For reasons that we shall come back to later, the inversion of the data was performed by using an atmospheric rotation period of 14.2 hr. This period corresponds to an eastward zonal wind velocity of 176 m/s relative to the magnetic field which rotates with a period of 16.11 hr (Warwick *et al.* 1989).

When the composition of the atmosphere is known, one may use the refractivity to determine the number density (n_i) of the gas. A recent study comparing infrared and radio occultation data acquired near the tropopause in the region probed during egress yielded a helium mole fraction of 0.190 ± 0.032 (Conrath *et al.* 1991). For the purpose of interpreting the occultation measurements, we have therefore adopted a He to H_2 abundance ratio of 19/81. In addition, we assume that aerosols and condensable vapors such as CH_4 , NH_3 , H_2S , and H_2O have a negligible effect on the microwave refractivity of the atmosphere above the 0.7 bar level. The latter assumption is based on vapor pressure considerations and on Voyager measurements of the aerosol and hydrocarbon distribution in Neptune's atmosphere (Rages & Pollack 1989; Broadfoot *et al.* 1989; Conrath *et al.* 1989). Empirical data relating gas density to refractivity were taken from Gennaoui (1951), Essen (1953), Maryott & Buckley

(1953), Nelson *et al.* (1967), Orcutt & Cole (1967), Bose *et al.* (1972), Spilker (1990), and the Chemical Rubber Company's Handbook of Chemistry and Physics. The resulting gas density is also shown in Fig. 3.

The next step in the interpretation of the refractivity profile consisted of determining the vertical pressure distribution in the atmosphere. It was computed for the case of hydrostatic equilibrium conditions by integrating the weight of the gas from the top of the detectable stratosphere and downward. Finally, the temperature was determined from the number density and the pressure by employing the equation of state given in the Appendix of an earlier report (Lindal *et al.* 1987). The gas compressibility factor was determined from data published by Reid *et al.* (1987). These assumptions and calculations yielded the ingress profile shown as a full drawn curve in Fig. 4. As can be seen from this profile, the tropopause, which was detected near the 100 mbar level, has a temperature of 52 ± 2 K, and the stratosphere has a temperature of 130 ± 12 K at 0.3 mbar. By comparison, Appleby (1986) and Orton *et al.* (1986) obtained tropopause temperatures of about 50 and 53 K, respectively, from studies of Neptune's brightness temperature spectrum, and Hubbard *et al.* (1987), who used stellar occultation data to study the thermal structure of the stratosphere, obtained a temperature of 135 K at 0.4 mbar for the case of solar-composition gas.

Below the tropopause, the temperature is increasing with depth. The methane mixing ratio is also expected to increase in this region and should, at some level below 1 bar, begin to contribute appreciably to the microwave refractivity of the gas. It is important to note, however, that the refractivity profile does not uniquely define the vertical changes in both the gas composition and the temperature. In order to handle this ambiguity and be able to determine the temperature and the methane distribution below the 1 bar level, it is therefore

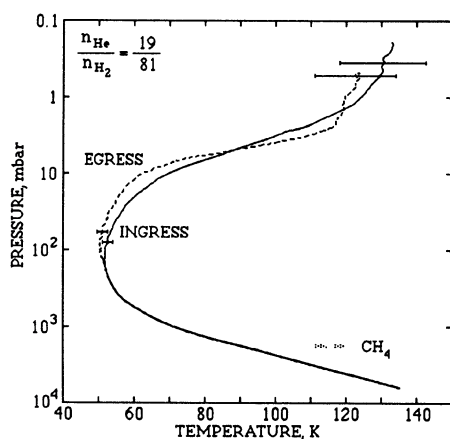


FIG. 4. Temperature vs pressure level in Neptune's stratosphere and troposphere. The solid curve corresponds to the nominal model, which was derived from ingress data acquired between 62° and 59° north latitude. The dashed curve was determined from measurements conducted between 45° and 38° south latitude during egress. Both datasets were obtained near the morning terminator. The profiles assume a helium to hydrogen abundance ratio of 19/81, and the error bars include the uncertainty in the composition.

necessary to introduce some auxiliary assumptions. As outlined below, the nominal model was developed by assuming that the region with the small refractivity scale height shown in an expanded view in the upper right-hand corner of Fig. 3, is a layer where the methane mixing ratio is decreasing rapidly with increasing altitude—and where condensation effects may cause haze to form. Although this layer appears to have been far from uniformly saturated with methane in the region probed during ingress, we shall for the purpose of discussion, refer to this region as a haze layer.

Between the top of the haze layer and the tropopause, the relative methane humidity, which we define here as the ratio between the partial pressure of methane and the saturation pressure of the vapor at the air temperature, was assumed to be constant and independent of altitude. With this auxiliary assumption, the refractivity data were employed to calculate the number density, pressure, and temperature distributions above the haze layer. Inside the haze layer, the refractivity profile was used to define the methane distribution. The temperature profile in this region was determined by assuming that the lapse rate is a linear function of the relative methane humidity and by interpolating between the dry and the wet adiabatic lapse rates expected from theory when H_2 is in “frozen equilibrium” (Houghton 1977). As is common in studies of outer planet atmospheres, the term “frozen equilibrium” is used here to describe the situation where the ortho to para H_2 abundance ratio is equal to the equilibrium ratio at the local temperature at each level in the atmosphere, and the rates of conversion between ortho and para states are too slow to have an appreciable effect on the adiabatic temperature lapse rate (Massie & Hunten 1982; Orton *et al.* 1986; Gierasch & Conrath 1987).

A constant relative humidity of 15% was adopted for the nominal model in the region between the tropopause and the haze layer. At the base of the layer, this yielded a relative humidity of 25% which is close to the maximum value that can be achieved by varying the relative humidity above the layer. The corresponding methane mixing ratio is 2% by number density. It should be noted that this methane mixing ratio represents an average over roughly a 100-km-long horizontal portion of the ray path that tangentially grazed the base of the layer where the pressure was 1.9 bars. As shown in Fig. 4, the temperature at the 1.9 bar level was about 92 K, which was approximately 9 K too high for this region to have been uniformly saturated with methane when the average mixing ratio was 2%. Thus, if the tracking link encountered haze at 60° north latitude, it apparently did so only at sporadic locations. Additional evidence indicating that the horizontal distribution of methane may have been far from uniform was provided by the signal spectra which show a variable frequency broadening while the link periapsis passed through this region.

The low relative humidity inferred from the ingress data may reflect local meteorological conditions such as, for instance, a downdraft bringing air depleted in CH_4 from higher elevations. If the CH_4 distribution on Neptune is as variable as the H_2O distribution in the terrestrial troposphere, the result obtained at 60° N might not provide a reliable indication of the average global CH_4 mixing ratio deep in Neptune's atmosphere. It is therefore interesting to compare the results reported here with data acquired with earth-based instruments that observe a larger region on the planet. For comparison, Orton *et al.* (1986) have derived a CH_4 mixing ratio of 2% based on measurements of Neptune's

brightness temperature in the submillimeter and millimeter portion of the spectrum, and Baines & Smith (1990) obtained a mixing ratio of 2.3%–3.7%.

Below the base of the haze layer, the methane mixing ratio was assumed to be constant, and the ammonia distribution was determined from the microwave absorption data by employing the algorithm published by Berge & Gulkis (1976). Except for the presence of NH_3 , which only has a small effect on the total gas number density, pressure, and temperature, the details of the profile calculations are similar to the approach used in an earlier study of Uranus (Lindal *et al.* 1987). Before being extinguished by absorption during ingress, the link reached down to a level where the nominal model has a pressure and temperature of 6.3 bars and 135 K, respectively. The ammonia mixing ratio at this level is 500 ± 150 parts per billion which indicates subsaturated conditions. At higher altitudes, the NH_3 distribution follows approximately the vapor saturation curve.

Besides the ambiguity introduced by the uncertainty in the methane distribution in the troposphere, the interpretation of the occultation measurements is also affected by a lack of reliable information on the rotation period of the atmosphere. The reason is that the rotation period is one of the parameters that determines the shape of the geoids which serve as iso-refractivity and absorptivity surfaces in the inversion process (see Appendix). The rotation period has a significant effect on the profile calculations below the 1.7 bar level because the latitudinal motion of the link periapsis becomes increasingly important below this pressure level.

The radio link first entered Neptune's stratosphere near 62° north. From there on, the link periapsis moved towards lower latitudes. Signal extinction occurred at about 59° north. No clouds were observed with the imaging system on Voyager 2 near these latitudes (Smith *et al.* 1989). It was therefore necessary to use the occultation data to establish reasonable bounds on the rotation period in this region. This approach yielded a period in the range of 13.9–14.5 hr. Increasing the rotation period above 14.5 hr changes the shape of the geoids that are used as iso-refractivity and absorptivity surfaces in the inversion process to such an extent that the ray-periapsis altitude, instead of being a monotonically de-

creasing function of time, reaches a minimum and then starts to increase before the signals are extinguished. Rotation periods longer than 14.5 hr are therefore incompatible with the ingress measurements if horizontal refractivity and absorptivity gradients are negligible near 60° north latitude. On the other hand, decreasing the rotation period causes the calculated depth of the measurements to increase considerably which, in turn, makes the refractivity scale height increase more rapidly with depth in the lowest region probed by the tracking link. When the rotation period is reduced below 13.9 hr, this effect produces a temperature profile with a superadiabatic lapse rate. Thus, rotation periods shorter than 13.9 hr can be ruled out at 60° north if the lowest region probed by the link is assumed to be stable against convection and have a constant methane mixing ratio. The nominal model was developed by adopting a rotation period of 14.2 hr which corresponds to the arithmetic mean of these two extremes. By comparison, cloud images obtained at 50° and 70° south latitude show atmospheric rotation periods scattered between 12.4 and 18 hr (Smith *et al.* 1989).

Figures 5 and 6 illustrate how the limits on the rotation period at 60° north may be used to establish bounds on the temperature and methane distributions in this region of the troposphere. The first of these figures shows two models labeled A and B that were obtained by inverting the ingress data with a constant rotation period of 14.5 hr, which corresponds to an eastward zonal wind velocity of 145 m/s relative to the magnetic field. Models C and D in Fig. 6 were developed by using a period of 13.9 hr, which is equivalent to a 208 m/s eastward zonal wind.

It should be noted here that the auxiliary assumptions used to calculate the temperature and methane distributions in the models depicted in Figs. 5 and 6 are similar to those employed in the development of the nominal model; i.e., the relative CH_4 humidity was taken to be constant between the tropopause and the layer with the small refractivity scale height, and below this layer the CH_4 mixing ratio was considered to be constant. Inside the layer with the small refractivity scale height the temperature lapse rate was assumed to be a linear function of the relative humidity and the CH_4 distribution was calculated from the refractivity profile. All

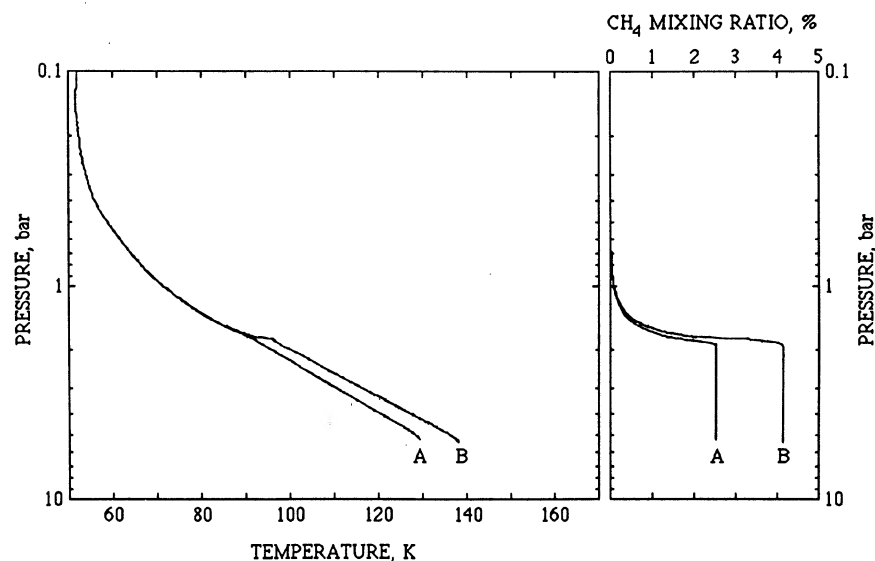


FIG. 5. Models for Neptune's troposphere. The profiles were computed from the ingress data by using an atmospheric rotation period of 14.5 hr, which corresponds to an eastward zonal wind velocity of 145 m/s relative to the magnetic field. Both models assume a helium to hydrogen abundance ratio of 19/81.

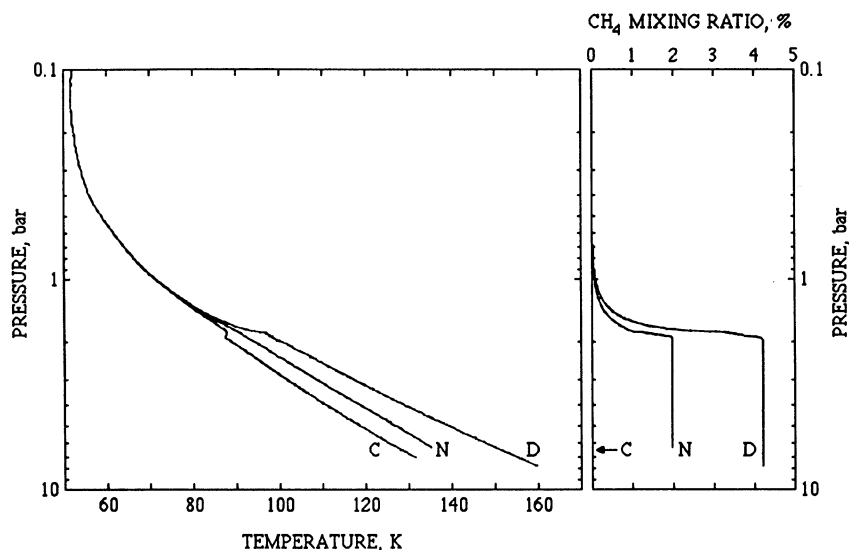


FIG. 6. Models for Neptune's troposphere. All three models were obtained from the ingress data by using a helium to hydrogen abundance ratio of 19/81. The profiles labeled C and D assume an atmospheric rotation period of 13.9 hr. These profiles provide lower and upper limits for the temperature and methane distribution near 60° north latitude. The profile labeled N corresponds to the nominal model, which was obtained by inverting the data with a rotation period of 14.2 hr.

the models contain ammonia, and the NH_3 mixing ratios were calculated from the microwave absorptivity profiles by using the algorithm developed by Berge & Gulkis (1976).

The particular assumptions used in the development of the models shown in Figs. 5 and 6 were chosen in order to provide upper and lower limits on the temperature and methane distribution. Before proceeding to a more detailed discussion of each of these models, it may be useful to briefly outline how changes in the distribution of CH_4 affect the tropospheric number density, pressure, and temperature profiles calculated from the occultation data. Methane, which is a nonpolar molecule, has an electric dipole polarizability that is about 3 times larger than that of H_2 and 13 times larger than He. Thus, increasing the CH_4 mixing ratio used in the models (which is done by increasing the relative CH_4 humidity in the region between the tropopause and the layer with the small refractivity scale height) has the effect of reducing the total gas number density calculated from the refractivity data. However, the total gas pressure in a predominantly hydrogen atmosphere is increased when the CH_4 mixing ratio is increased because the molecular mass of CH_4 is 8 times greater than that of H_2 . The result of all this is that the gas temperature calculated from the occultation data is increased when the CH_4 mixing ratio is increased. More information concerning the calculation of gas number density, pressure, and temperature profiles from radio occultation data is available in the Appendix of an earlier report (Lindal *et al.* 1987).

Model A in Fig. 5 was derived by assuming that the troposphere was saturated with ammonia at the lowest level probed with the tracking link. This boundary condition puts a constraint on the temperature and therefore also on the methane distribution in the troposphere. The profiles calculated for model A extend down to the 5.2 bar level where the temperature is 130 K and the ammonia and methane mixing ratios are 0.6×10^{-6} and 0.025, respectively. In this model, the ammonia distribution follows approximately the vapor saturation curve. Reducing the amount of methane leads to lower gas temperatures and supersaturated NH_3 vapor. Thus, model A provides reasonable lower bounds on the temperature and CH_4 mixing ratio for the case of an atmospheric rotation period of 14.5 hr.

The model labeled B in Fig. 5 was obtained by using the maximum methane relative humidity that can be accommodated above the layer with the small refractivity scale height before the temperature increases so much that methane becomes the principal constituent in the troposphere. Thus, model B provides upper limits on the temperature and methane mixing ratio for the case of an atmospheric rotation period of 14.5 hr. The profiles computed for this model extend down to the 5.4 bar level where the temperature is 138 K, and the methane and ammonia mixing ratios are 0.04 and 0.7×10^{-6} , respectively. In this case, NH_3 does not saturate at any level.

Model B has a region with a superadiabatic lapse rate near the 1.7 bar level. It should be noted, however, that this region is not convectively unstable because the mixing ratio of CH_4 drops rapidly with increasing altitude. A derivation of the stability criterion applicable to this situation is available in the Appendix of a previous paper (Lindal *et al.* 1987).

Figure 6 shows the nominal model (labeled N) discussed previously plus two models C and D that were developed by inverting the ingress data with a rotation period of 13.9 hr. Here model C was obtained by assuming that the methane abundance is negligible. The layer with the small refractivity scale height is instead interpreted in terms of a thermal inversion. In this model, the pressure at the lowest level reached by the tracking link is 7 bars. The temperature and ammonia mixing ratio at this level are 132 K and 0.4×10^{-6} , respectively. The ammonia vapor is not saturated at the 7 bar level but becomes supersaturated at higher altitudes. Model C provides absolute lower bounds on the temperature and methane distribution in the ingress region, and the only way one can reduce the gas temperature further is by reducing the helium mixing ratio below the 0.19 value assumed in this paper.

Model D in Fig. 6 provides upper limits on the temperature and CH_4 distribution in the troposphere. It was developed by adopting the maximum relative methane humidity that can be used above the layer with the small refractivity scale height without increasing the temperature so much that methane becomes the principal constituent in the troposphere. At the lowest level probed with the tracking link, this model has a pressure of 7.7 bars and a temperature of 160 K.

The corresponding ammonia and methane mixing ratios are 0.5×10^{-6} and 0.04, respectively. In this model, NH_3 is not saturated at any level. As illustrated in Fig. 6, neither the rotation period nor the methane distribution have a significant effect on the computed temperature profiles above the 1 bar level.

Up to this point, we have confined our discussion to the ingress measurements because they are easier to interpret than the egress data. The stippled curve in Fig. 4 shows the temperature profile computed from egress data acquired between 45° and 38° south latitude. This profile extends down to the 1.6 bar level and was calculated by using an atmospheric rotation period of 17 hr which corresponds to a westward zonal wind velocity of about 100 m/s. Below this pressure level, the calculated profiles are very sensitive to variations in the zonal wind velocities in the latitude region between 38° and 15° south. The egress data are therefore not well suited for studying the thermal structure and composition below the 1.6 bar level. However, if one assumes that the vertical temperature and methane profiles between 38° and 15° south are similar to the nominal ingress profiles below the 1.6 bar level and that horizontal gradients are negligible, one may use the Doppler frequency data to estimate the zonal wind velocities in this latitude range. To the south of 35° latitude, this approach yielded a westward zonal wind velocity of roughly 100 m/s. Further to the north, the velocities are higher and appear to reach about 400 m/s near 15° south latitude. It is not clear, however, whether these zonal wind changes represent latitudinal or vertical wind shear. By comparison, cloud motion data acquired with the cameras on board Voyager 2 show westward winds with velocity values scattered between 50 and 600 m/s in the 38° to 15° latitude range (Smith *et al.* 1989). However, the velocities of the largest cloud features observed over the longest time intervals are within about 100 m/s of the estimates obtained from the egress data. Because of the uncertain structure of the atmosphere between 38° and 15° south, the signal intensity measurements in this region are not suitable for studying the ammonia distribution.

The nominal gas state profiles derived from the radio occultation measurements extend over an altitude interval of about 300 km and a pressure range from 0.3 mbar to 6.3 bars. Microwave absorption limited the depth of the measurements in the troposphere. The accuracy of the pressure and temperature profiles calculated from the data acquired below the 1 bar level was affected by uncertainties in the methane distribution and the rotation period of the atmosphere. The height to which the gas state profiles could be reliably determined in the stratosphere was limited by the stability of the spacecraft oscillator and by scintillations in the ionosphere which produced spectral broadening of the received signals.

In addition to determining the thermal structure and composition of the atmosphere, one may use the radio occultation measurements to study atmospheric dynamics and stratospheric waves. This is done by analyzing the amplitude and phase scintillations produced by small scale spatial refractivity irregularities encountered by the tracking link (Hinson & Tyler 1983; Hinson 1986; Hinson & Eshleman 1988). The scintillation measurements in Neptune's atmosphere are the subject of another investigation and will not be discussed here.

Another application of the radio data concerns the study of the physical size and shape of Neptune. Figure 7 illus-

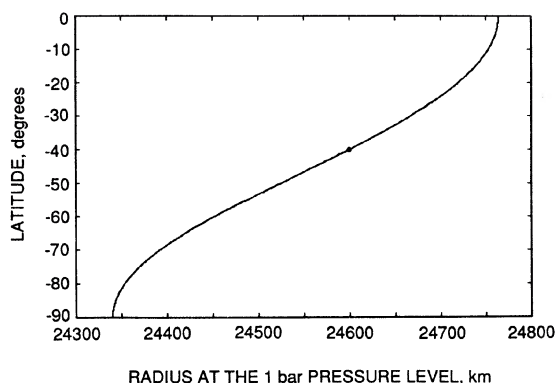


FIG. 7. Radius at the 1 bar pressure level vs planetocentric latitude in the southern hemisphere of Neptune. The discrete point corresponds to the radius observed during egress, and the curve through this point represents the geoid determined from the external gravity field (GM , J_2 , and J_4) and the atmospheric rotation periods observed with Voyager 2 (Hammel *et al.* 1989; Smith *et al.* 1989). The radius is measured from the center of mass.

trates the result of calculating the radius at the 1 bar pressure level in Neptune's southern hemisphere. The discrete point shown near 40° south latitude represents the 1 bar radius determined from the egress data. The curve through this point was determined by assuming that the isobaric surface is everywhere orthogonal to the local vertical which, in turn, is defined by the gravity field (GM , J_2 , and J_4) and the atmospheric rotation periods observed with Voyager 2 (Hammel *et al.* 1989; Smith *et al.* 1989). A detailed description of the method used to calculate the shape of the isobaric surface is available in the Appendix. The 1 bar surface has an equatorial radius of $24\,766 \pm 15$ km and a polar radius of $24\,342 \pm 30$ km, and the corresponding oblateness is 0.0171 ± 0.0014 . The errors in the computed radii are mostly due to the scatter in the observed cloud rotation periods (Smith *et al.* 1989).

Finally, one may use the occultation data to study Neptune's ionosphere. Figures 8 and 9 show the vertical electron number density profiles obtained by inverting the differential dispersive Doppler data acquired at DSS 43. As in the study of the neutral portion of the atmosphere, horizontal refractivity gradients were assumed to be negligible. The results suggest that there is an extended ionized region with a large scale height and a low plasma density above the 2500 km level. This altitude region is difficult to observe with the occultation experiment, however, because the small phase changes it produces on the tracking link are easily masked by the effects of spatial and temporal plasma variations in the terrestrial ionosphere and the interplanetary medium. Thus, the topside measurements may not be very accurate.

During the time intervals when the periapsis of the tracking link passed through the lower regions of Neptune's ionosphere, the wideband recordings show several short and abrupt dispersive Doppler fluctuations. These features in the recordings were probably caused by refraction as the link periapsis moved through either dense horizontally elongated patches of ionization or thin horizontally stratified layers. Similar effects were observed on Jupiter, Saturn, and Uranus. Figure 9 shows an expanded view of Neptune's lower

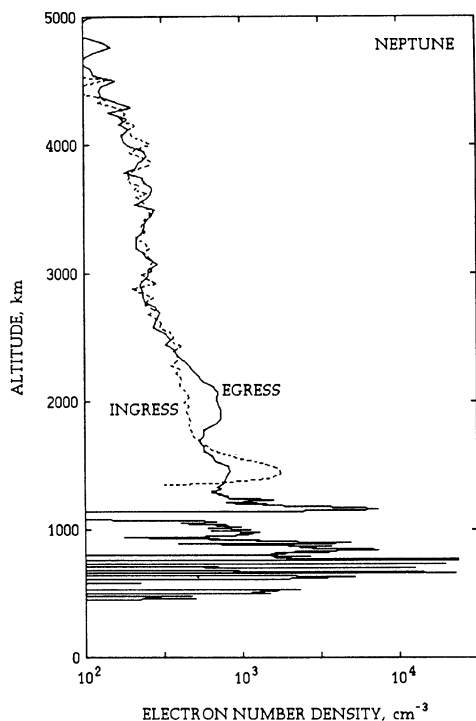


FIG. 8. Vertical distribution of free electrons in Neptune's ionosphere. The calculation assumes that horizontal plasma variations are negligible. Both profiles were obtained near the morning terminator. The altitude is measured from the 1 bar pressure level.

ionosphere. Note that the altitude regions where the profile shows a negative electron number density may be the result of deviations from horizontal plasma stratification or a failure to fully resolve the abrupt Doppler changes recorded

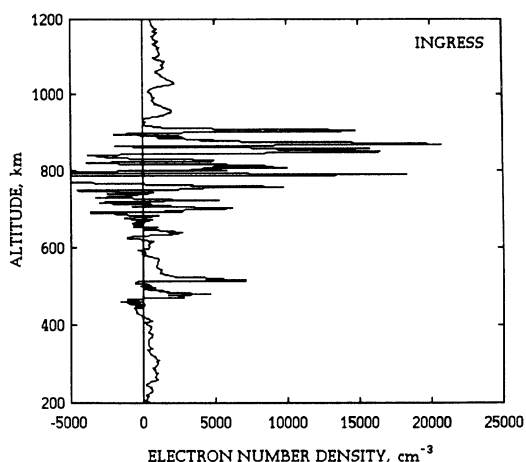


FIG. 9. Vertical distribution of free electrons in the lower ionosphere of Neptune. The profile was calculated from the dispersive Doppler data by assuming that horizontal plasma variations are negligible. Negative number densities indicate a deviation from horizontal plasma stratification or a failure to fully resolve the abrupt Doppler variations recorded with the wideband receiver channels. The altitude is measured from the 1 bar level.

with the wideband receiver channels. The densities calculated in the lower ionosphere are therefore quite uncertain.

3. DISCUSSION

In a recent paper discussing the radio brightness spectrum of Neptune, de Pater *et al.* (1991) suggest that hydrogen sulfide might be an important microwave absorber deep in Neptune's troposphere. Hydrogen sulfide, which is a polar molecule, does not appear to have been detected in the infrared spectra of any of the giant planets (Owen 1977; Fink & Larson 1979; Bézard *et al.* 1983; Larson *et al.* 1984; Prinn *et al.* 1984; Fegley *et al.* 1991). The electric dipole moment of the H_2S molecule is about half that of H_2O (Boggs *et al.* 1957; Nelson *et al.* 1967). By adopting the Debye approximation for the refractivity of H_2S and the absorption coefficient algorithm developed by de Pater *et al.* (1991), we have compared the expected effects of H_2S and NH_3 vapors. The results suggest that H_2S vapor was not the principal microwave absorber in the region probed during ingress because the required mixing ratio is so large that H_2S would have produced a detectable change in the refractivity scale height. Since no such scale height change was seen, the signal attenuation observed on the Voyager link was probably caused mostly by NH_3 vapor.

Figure 10 and Table 1 compare Neptune's nominal temperature profile with the results of previous Voyager occultation measurements. In the case of Neptune, Saturn, and Jupiter, whose profiles are shown as solid curves, the depth of the occultation measurements was limited by microwave absorption, and the signal attenuation allowed the ammonia mixing ratios to be determined. The stippled curve shows the result obtained at Uranus. Ammonia was not detected with the radio occultation measurements at Uranus because the spacecraft trajectory prevented the link from probing deep

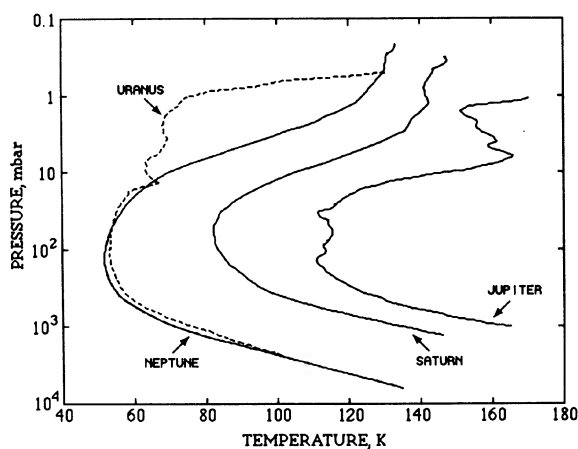


FIG. 10. Temperature profiles for the giant planets derived from radio occultation data acquired with the Voyager spacecraft. On Neptune, Saturn, and Jupiter, the depth of the measurements was limited by microwave absorption. In the case of Uranus, the depth was limited by the spacecraft trajectory which did not allow link bending angles greater than 3° to be observed. The measurements at Neptune were conducted near 60° north latitude, and the Uranian atmosphere was probed near the equator. The data for Saturn and Jupiter were obtained at latitudes of 36° north and 12° south, respectively. As discussed by Allison (1982, 1990), the Jovian temperature distribution may have been affected by vertically propagating atmospheric waves.

TABLE 1. Atmospheric data.

Pressure (mbar)	Jupiter	Temperature (K)			Pressure (mbar)	Jupiter	Temperature (K)		
		Saturn	Uranus	Neptune			Saturn	Uranus	Neptune
0.35				130.6	56.23	115.3	82.1	53.5	53.6
0.40				130.1	63.10	115.4	82.1	53.4	53.2
0.45				130.2	70.79	114.6	82.4	53.4	52.7
0.50			129.0	129.8	79.43	113.7	82.6	53.3	52.5
0.56		143.0	116.2	128.7	89.13	112.8	82.8	53.2	52.1
0.63		142.2	103.5	127.8	100.00	113.5	83.4	53.0	51.8
0.71		141.3	96.4	127.1	112.20	112.9	84.1	53.0	51.8
0.79		141.2	88.8	126.2	125.89	111.4	84.9	53.1	51.7
0.89		141.3	80.8	125.0	141.25	110.9	85.7	53.4	51.7
1.00	169.1	141.6	76.4	123.9	158.49	111.7	86.8	53.5	51.8
1.12	168.8	142.1	73.9	122.9	177.83	112.9	88.2	53.9	52.1
1.26	160.7	142.5	72.8	121.5	199.53	114.1	89.8	54.3	52.3
1.41	152.8	141.5	71.6	119.6	223.87	115.7	91.1	54.7	52.6
1.58	151.4	140.3	70.3	117.1	251.19	117.4	92.4	55.2	53.1
1.78	152.3	139.0	69.1	114.6	281.84	119.5	93.8	55.7	53.6
2.00	154.9	137.7	68.5	112.3	316.23	121.2	95.6	56.3	54.3
2.24	156.0	137.3	68.2	109.9	354.81	123.8	97.9	57.2	55.1
2.51	155.5	136.9	68.0	106.9	398.11	127.2	100.7	58.3	56.0
2.82	156.6	135.9	68.3	103.2	446.68	130.1	103.9	59.6	57.2
3.16	158.8	133.4	68.8	100.4	501.19	132.5	107.5	61.3	58.8
3.55	160.6	131.2	69.4	97.6	562.34	136.9	111.6	63.2	60.6
3.98	161.4	129.0	69.0	94.4	630.96	142.4	115.8	65.3	62.4
4.47	159.0	126.2	68.4	90.9	707.95	146.9	120.3	67.6	64.3
5.01	160.5	123.5	67.9	87.4	794.33	151.2	125.0	70.3	66.4
5.62	164.0	120.6	67.0	84.1	891.25	157.5	129.9	73.2	68.7
6.31	165.9	117.7	64.8	80.9	1000.00	165.0	134.8	76.4	71.5
7.08	163.0	114.8	63.8	77.7	1122.02		139.9	80.1	74.5
7.94	159.5	112.0	63.4	74.9	1258.93		145.0	82.9	77.9
8.91	154.8	108.4	63.3	72.3	1298.48		146.2	83.5	78.7
10.00	147.0	104.8	63.4	69.7	1412.54			85.9	81.4
11.22	140.4	102.2	64.3	67.6	1584.89			89.2	85.8
12.59	133.5	99.5	65.9	65.9	1778.28			92.6	90.3
14.13	129.2	97.3	66.2	64.3	1995.26			96.0	94.4
15.85	124.9	95.0	61.1	62.8	2238.72			99.8	98.4
17.78	121.9	92.7	58.8	61.5	2308.81			100.9	99.4
19.95	119.9	90.5	58.2	60.4	2511.89				102.2
22.39	118.1	88.7	57.2	59.2	2818.38				106.3
25.12	116.6	87.0	56.4	58.3	3162.28				110.4
28.18	115.6	85.6	55.7	57.5	3548.13				114.5
31.62	111.7	84.2	55.2	56.7	3981.07				118.7
35.48	111.4	83.8	54.9	56.0	4466.84				122.9
39.81	113.0	83.3	54.6	55.3	5011.87				127.2
44.67	114.2	82.8	54.3	54.7	5623.41				131.2
50.12	114.6	82.3	53.9	54.1	6267.92				135.0

enough in the troposphere. At the lowest level probed, the temperature was only about 101 K, and at that temperature the NH_3 vapor pressure is too low to produce detectable absorption at the frequencies transmitted from the Voyager spacecraft.

As one would expect, Fig. 10 shows that the tropospheric temperatures increase significantly as one moves closer and closer to the sun. One exception is Uranus, which, due to its weak internal heat source, is almost as cold as Neptune. Another effect illustrated in the figure is that the tracking links probed deeper in the cold tropospheres than in the warm ones. The reason is presumably that ammonia is being frozen out at a lower level in the cold atmospheres.

Table 2 summarizes some of the more significant atmospheric results obtained from the radio occultation measurements conducted at the giant planets.

The acquisition of the radio occultation data discussed in this article was accomplished through the coordinated efforts of the Voyager Project Staff, the Deep Space Net personnel, the Radio Science Support Team, and the Radio Science Team. The science and support teams consisted of V. R. Eshleman, D. L. Gresh, E. M. Gurrola, D. P. Hinson, E. A. Marouf, P. A. Rosen, R. A. Simpson, and G. L. Tyler (science team leader) from Stanford University, N. Kawa-

shima from the Institute of Space and Astronautical Sciences, and J. D. Anderson, S. W. Asmar, S. E. Borutzki, J. K. Campbell, M. L. Delitsky, A. C. Densmore, P. M. Eshe, E. R. Kursinski, G. S. Levy, G. F. Lindal, J. R. Lyons, D. D. Morabito, Y. H. Son, D. N. Sweetnam (support team leader), and G. E. Wood from the Jet Propulsion Laboratory. Asmar, Lyons, and Sweetnam provided support in the reduction of the wide band recordings, and the Voyager Navigation Team supplied the ephemerides required to invert the data. J. Lindal checked the derivations of the equations given in the Appendix, and I. de Pater provided the algorithm that was used in estimating the microwave absorptivity of hydrogen sulfide. Two anonymous referees provided helpful suggestions and advice regarding the presentation of the material. The analysis reported here was carried out at the Jet Propulsion Laboratory of the California Institute of Technology under contract with the National Aeronautics and Space Administration.

APPENDIX: RAY TRACING INVERSION

Several analytical and numerical inversion techniques have been developed for the analysis of radio occultation data acquired in oblate planetary atmospheres. This appendix describes a method that is based on the tracing of rays.

TABLE 2. Physical data on Jupiter, Saturn, Uranus, and Neptune.

	Jupiter	Saturn	Uranus	Neptune
Magnetic field rotation period ^a	9 hr 55 min 29.7s	10 hr 39 min 22.4 s	17.24 hr	16.11 hr
At the 1 bar pressure level:				
Radius (km)				
Equatorial	71 492 ± 4	60 268 ± 4	25 559 ± 4	24 766 ± 15
Polar ^b	66 854 ± 10	54 364 ± 10	24 973 ± 20	24 342 ± 30
Oblateness ($R_{eq} - R_p$)/ R_{eq}	0.06487 ± 0.00015	0.09796 ± 0.00018	0.02293 ± 0.00080	0.0171 ± 0.0014
Acceleration of gravity (m/s ²)				
Equatorial ^c	23.12 ± 0.01	8.96 ± 0.01	8.69 ± 0.01	11.00 ± 0.05
Polar	27.01 ± 0.01	12.14 ± 0.01	9.19 ± 0.02	11.41 ± 0.03
Atmospheric temperature ^d (K)	165 ± 5	134 ± 4	76 ± 2	72 ± 2

^a From Davies *et al.* (1986) and Warwick *et al.* (1986; 1989).

^b For Jupiter and Saturn, the polar radii are average values for the north and south poles. In the case of Uranus and Neptune, the values given here represent extrapolations to the south pole.

^c Values apply to objects corotating with the atmospheric gas.

^d Temperature values assume that the atmospheres of Jupiter, Saturn, Uranus, and Neptune consist of 89% ± 3%, 94% ± 3%, 85% ± 3%, and 81% ± 3% hydrogen, respectively, with the remainder being mostly helium.

In order to determine the vertical changes in the refractive index and the absorption coefficient of an atmosphere from a single ingress or egress dataset, one must first make some assumptions about the horizontal variations in these gas parameters in the regions probed by the radio link. The approach discussed below assumes that the absorption coefficient and the refractive index are constant along geoids. Here a geoid is defined as a surface that is everywhere orthogonal to the local vertical. Thus, the gradients of the refractive index and the absorption coefficient of the atmosphere are, by assumption, colinear with the acceleration of gravity (\mathbf{g}) that would be experienced by an observer moving with the gas. It should be noted, however, that this approach will not always yield accurate vertical profiles because both the total number density and the concentrations of minor condensable constituents such as CH₄, NH₃, and H₂O may vary along the geoids in the regions probed by the radio link.¹ However, the errors caused by horizontal changes can be minimized by designing the occultation experiment so that the spacecraft is setting and rising approximately perpendicular to the limb of the planet as viewed from the Earth.

Radio tracking data acquired with Pioneer and Voyager spacecraft indicate that the external gravity fields of the out-

¹In the ideal case of a fluid planet with uniform composition, constant pressure along geoids, and axially symmetric continuous rotation (i.e., no meridional circulation and vortices or other weather systems but strictly inviscid zonal circulation), one can by employing the hydrodynamic equations show that the gradient of the refractivity lies in the meridian plane and is inclined with respect to the local vertical. If the inclination angle $\delta(r, \varphi)$ is measured in radians and defined as positive when the refractivity gradient is tilted away from the vertical in the northerly direction (where north is defined in terms of the angular velocity vector), one obtains

$$\delta(r, \varphi) \approx \frac{8\pi^2 H_N r \cos^2 \varphi}{g T_R^3} \left(\frac{1}{r} \frac{\partial T_R}{\partial \varphi} + \frac{\partial T_R}{\partial r} \tan \varphi \right),$$

where the independent variables r and φ are the position coordinates defined in Fig. 11, H_N is the refractivity scale height, g is the acceleration of gravity, and T_R is the rotation period of the fluid.

Radial and latitudinal wind shear data obtained from recent Voyager observations (Flasar *et al.*, 1987; Smith *et al.*, 1989), indicate that $\delta(r, \varphi)$ is negligible at most latitudes on the outer planets. Thus, in atmospheric regions with predominantly zonal circulation, uniform composition, and constant pressure along the geoids, horizontal refractivity variations should normally have a negligible effect on the accuracy of vertical profiles derived from occultation data.

er planets are symmetric with respect to the spin axes, as one would expect in the case of rotating objects consisting mostly of fluids. When the atmospheric winds are assumed to be zonal, \mathbf{g} is a vector contained in the local meridian plane. One can therefore express \mathbf{g} as the sum of two components:

$$\mathbf{g} = \mathbf{u}_r g_r + \mathbf{u}_\varphi g_\varphi, \quad (1)$$

where \mathbf{u}_r and \mathbf{u}_φ are the unit vectors in the radial and latitudinal directions, respectively, and g_r and g_φ are given by

$$g_r(r, \varphi) = -\frac{GM}{r^2} + \frac{2}{3} \omega^2 r [1 - P_2(\sin \varphi)] + \frac{GM}{r^2} \sum_{i=1}^{\infty} (2i+1) J_{2i} \left(\frac{R_J}{r} \right)^{2i} P_{2i}(\sin \varphi), \quad (2)$$

$$g_\varphi(r, \varphi) = -\frac{1}{3} \omega^2 r \frac{dP_2(\sin \varphi)}{d\varphi} - \frac{GM}{r^2} \sum_{i=1}^{\infty} J_{2i} \left(\frac{R_J}{r} \right)^{2i} \frac{dP_{2i}(\sin \varphi)}{d\varphi}. \quad (3)$$

In these expressions, the independent variables r and φ denote the distance from the center of mass and the planetocentric latitude, respectively (cf. Fig. 11). Among the remaining parameters, G is the universal gravitational constant, M is the mass of the planet, J_{2i} is the 2*i*th zonal harmonic coefficient, R_J is the radius to which the zonal harmonic coefficient

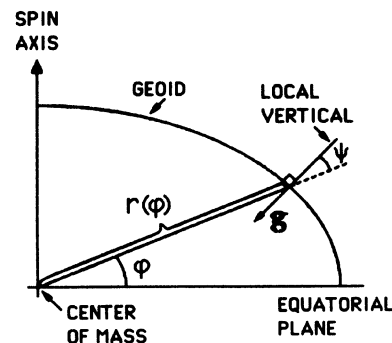


FIG. 11. Geometric properties of geoids.

TABLE 3. Gravity field parameters for the giant planets.

	$GM \times 10^{-7}$ ($\text{km}^3 \text{s}^{-2}$)	$J_2 \times 10^2$	$J_4 \times 10^4$	$J_6 \times 10^4$	R_J (km)	References
Jupiter	12.6686538 ± 0.0000100	1.4697 ± 0.0001	- 5.84 ± 0.05	0.31 ± 0.20	71,492	Campbell & Synnott 1985
Saturn	3.7931272 ± 0.0000200	1.6332 ± 0.0010	- 9.19 ± 0.40	1.04 ± 0.50	60,268	Campbell & Anderson 1989
Uranus	0.5793947 ± 0.0000023	0.35160 ± 0.00032	- 0.354 ± 0.041	—	25,559	French <i>et al.</i> 1986 Anderson <i>et al.</i> 1987
Neptune	0.6835096 ± 0.0000021	0.3539 ± 0.0010	- 0.28 ± 0.22	—	24,766	Tyler <i>et al.</i> 1989

cients have been normalized, P_{2i} is the Legendre polynomial of degree $2i$, and ω is the angular velocity of the gas in the atmospheric region under study.

A summary of relevant gravity field parameters for the giant planets is given in Table 3. Note that the values of the zonal harmonic coefficients have been normalized to the 1 bar equatorial radii. All the tabulated results were obtained from spacecraft data, with the exception of J_2 and J_4 for Uranus which were determined by studying the precession of the Uranian rings (French *et al.* 1986).

For the three first Legendre polynomials that appear in Eqs. (2) and (3), one has

$$P_2(\sin \varphi) = \frac{1}{2}(3 \sin^2 \varphi - 1), \quad (4)$$

$$P_4(\sin \varphi) = \frac{1}{8}(35 \sin^4 \varphi - 30 \sin^2 \varphi + 3), \quad (5)$$

$$P_6(\sin \varphi) = \frac{1}{16}(231 \sin^6 \varphi - 315 \sin^4 \varphi + 105 \sin^2 \varphi - 5), \quad (6)$$

and ω is given by

$$\omega(r, \varphi) = \omega_{mf} + \frac{v_w}{r \cos \varphi}, \quad (7)$$

where ω_{mf} is the angular velocity of the magnetic field, which can be calculated from the rotation periods given in Table 2, and v_w is the zonal wind velocity relative to the magnetic field. Note that v_w is defined positive in the direction that the magnetic field is rotating. In the case of Neptune's atmosphere, Smith *et al.* (1989) give v_w as a function of the planetographic latitude which is simply equal to $(\varphi + \psi)$, where ψ is defined in Fig. 11 and given by

$$\psi = \arctan\left(\frac{g_\varphi}{g_r}\right). \quad (8)$$

The ray tracing inversion technique is based on the concept that each Doppler frequency sample in the dataset to be inverted corresponds to a ray or photon trajectory that begins at the point (P_1) in space where the spacecraft was located at the time of transmission and ends at the point (P_3) where the tracking station was at the time of reception (cf. Fig. 12). In what follows, we shall refer to these rays as sampling rays. By starting with a ray grazing the top of the atmosphere and proceeding downward to lower and lower rays, the refractive index at the levels corresponding to the lowest geoid reached by each ray is determined in a sequential manner so that each photon arrives at the tracking station with the observed frequency. Thus, when the inversion process is completed, one has a series of geoids where the refractive index of the atmosphere has been determined. In what follows, we shall refer to these geoids as sampling geoids.

The frequency of the photon arriving at the tracking station may be calculated from

$$f_R = f_T \frac{\sqrt{1 - (v_1/c)^2}}{1 - (v_1/c) \cos \phi_1} \left(1 + \frac{\Delta U_N}{c^2}\right) \frac{1 - (v_2/c) \cos \phi_2}{\sqrt{1 - (v_2/c)^2}}, \quad (9)$$

where c is the velocity of light in vacuum, and f_T is the frequency radiated from the spacecraft antenna as measured by an observer at rest on the spacecraft. The spacecraft transmitter frequency may be determined from tracking data acquired before and after the atmospheric measurements.

Among the remaining parameters in Eq. (9), v_1 denotes the velocity of the spacecraft at the time the photon is leaving for the Earth and ϕ_1 is the angle between the spacecraft's and the photon's velocity vectors. Similarly, v_2 is the velocity of the station at the time the photon is received, and ϕ_2 is the corresponding angle between the velocity vectors of the arriving photon and the station. The parameters v_1 , ϕ_1 , v_2 , and ϕ_2 are calculated in an inertial reference frame at rest with respect to the center of mass of Neptune at the time the photon passes through the atmosphere. The term $\Delta U_N/c^2$ accounts for the gravitational frequency shift expected from the general theory of relativity. Here ΔU_N denotes the difference between the Newtonian gravity potentials at the spacecraft and at the tracking station. Because of the dominating effect of the sun's gravity field, ΔU_N was positive during the Neptune encounter—thereby giving rise to a gravitational blue shift.

Finding the ray solution for a new Doppler data sample requires many numerical operations since it is necessary to solve for both the direction in which to launch the ray from the spacecraft and the refractive index gradient near the ray periaapsis. In order to reduce the number of ray tracing trials required to obtain the correct solution for each sampling ray, it is therefore desirable to first determine the approximate direction in which each photon should be launched from the spacecraft before actually starting to trace rays through the

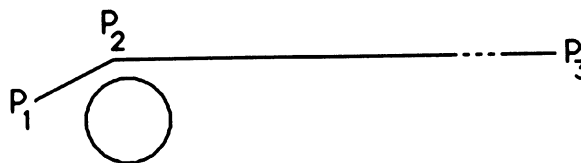


FIG. 12. Approximate ray path consisting of two straight line segments P_1P_2 and P_2P_3 . Here P_1 represents the location of the spacecraft at the time of photon transmission, P_2 a point in the atmosphere satisfying the three criteria discussed in the text, and P_3 the position of the tracking station at the time of reception.

atmosphere. This may be done by solving for the approximate ray path illustrated in Fig. 12 which simply consists of two straight line segments connecting the three points P_1 , P_2 , and P_3 . Here, P_2 denotes a point in the atmosphere that is being illuminated by the spacecraft's antenna beam, and that satisfies the following three criteria:

(1) The local vertical at point P_2 lies in the plane \mathcal{R} which we define as the plane containing the three points P_1 , P_2 , and P_3 .

(2) The local vertical at P_2 bisects the angle between the line segments P_2P_1 and P_2P_3 .

(3) A photon traveling along the path $P_1P_2P_3$ arrives at the tracking station with the recorded frequency.

The location of the point P_2 may be obtained with an iterative numerical procedure. The procedure can be started by first making an initial guess regarding the location of P_2 based, for example, on the final solution for the previous ray. Next, a determination must be made of the errors (ϵ_1 , ϵ_2 , and ϵ_3) that need to be corrected before the three criteria given above are satisfied. With regard to criterion 1, this involves computing the angle (ϵ_1) between the local vertical at P_2 and the plane \mathcal{R} . In the case of criterion 2, one computes the angle (ϵ_2) between the projection of the local vertical at P_2 into the \mathcal{R} plane and the line bisecting the angle between the two line segments P_2P_1 and P_2P_3 . The error in the Doppler shifted frequency of a photon arriving at P_3 via the $P_1P_2P_3$ path (ϵ_3) is determined by subtracting the frequency recorded at the tracking station from the frequency obtained by using Eq. (9).

The next step in the procedure involves linearizing the relationship between the errors defined above, and the orthogonal vector components of a small displacement ($\Delta\xi, \Delta\eta, \Delta\zeta$) of P_2 relative to its initial position. This requires that the partial derivatives of ϵ_1 , ϵ_2 , and ϵ_3 with respect to ξ , η , and ζ be determined numerically. Finally, a new and improved location is obtained for P_2 by solving the following linear system of equations with regard to $\Delta\xi$, $\Delta\eta$, and $\Delta\zeta$:

$$\begin{pmatrix} \epsilon_1 \\ \epsilon_2 \\ \epsilon_3 \end{pmatrix} + \begin{pmatrix} \frac{\partial \epsilon_1}{\partial \xi} & \frac{\partial \epsilon_1}{\partial \eta} & \frac{\partial \epsilon_1}{\partial \zeta} \\ \frac{\partial \epsilon_2}{\partial \xi} & \frac{\partial \epsilon_2}{\partial \eta} & \frac{\partial \epsilon_2}{\partial \zeta} \\ \frac{\partial \epsilon_3}{\partial \xi} & \frac{\partial \epsilon_3}{\partial \eta} & \frac{\partial \epsilon_3}{\partial \zeta} \end{pmatrix} \begin{pmatrix} \Delta\xi \\ \Delta\eta \\ \Delta\zeta \end{pmatrix} = \begin{pmatrix} 0 \\ 0 \\ 0 \end{pmatrix}, \quad (10)$$

This procedure is repeated until the location of P_2 is established with the desired accuracy.

The line segment P_1P_2 gives the approximate direction in which a photon must be launched from the spacecraft if it is to reach the tracking station with the observed frequency. However, in order to find the actual path of the photon, one must account for refraction and step by step trace the ray through the atmosphere. This process requires that one utilizes the differential equation for the ray, which may be expressed as

$$\frac{d}{ds} \left(n \frac{d\mathbf{p}}{ds} \right) = \text{grad}(n), \quad (11)$$

where $d\mathbf{p}$ denotes an elemental displacement vector along the ray, ds the length of this displacement vector, and n the refractive index of the atmosphere. The time it takes the photon to traverse the distance ds is given by nds/c , where c is the speed of light in vacuum.

For the purpose of determining the shape of the ray segments that make up the steps along the path through the atmosphere, we will use the Cartesian coordinate system depicted in Fig. 13. The origin of this system was chosen so that it coincides with the starting point of the ray segment. At the origin, the x axis is tangential to the ray and the xy plane contains the refractive index gradient. The xy plane is therefore the osculating plane of the ray at the origin. Relative to the center of mass of the planet, the position of the photon is given by $\mathbf{r}_0 + \mathbf{p}$. Here \mathbf{r}_0 denotes the vector from the center of mass to the origin of the Cartesian coordinate system in Fig. 13.

In order to solve Eq. (11), we now express \mathbf{p} in terms of its Cartesian vector components:

$$\mathbf{p} = u_x x + u_y y(x) + u_z z(x), \quad (12)$$

where u_x , u_y , and u_z are the unit vectors in the x , y , and z directions, respectively. Here $y(x)$ represents the deflection of the ray path due to refraction in the osculating plane, and $z(x)$ the effect of ray torsion due to the oblateness of the atmosphere. For the unit vector tangential to the ray, one obtains

$$\frac{d\mathbf{p}}{ds} = (u_x + u_y y' + u_z z') \frac{dx}{ds}. \quad (13)$$

Here y' and z' denote the derivatives of y and z with respect to x , and dx/ds is given by

$$\frac{dx}{ds} = \frac{1}{\sqrt{1 + (y')^2 + (z')^2}}. \quad (14)$$

By using Eqs. (13) and (14), one can now rewrite Eq. (11) as follows:

$$\begin{aligned} & u_x \left[\frac{\partial n}{\partial x} - \frac{1}{\sqrt{1 + (y')^2 + (z')^2}} \frac{d}{dx} \left(\frac{n}{\sqrt{1 + (y')^2 + (z')^2}} \right) \right] \\ & + u_y \left[\frac{\partial n}{\partial y} - \frac{1}{\sqrt{1 + (y')^2 + (z')^2}} \frac{d}{dx} \left(\frac{ny'}{\sqrt{1 + (y')^2 + (z')^2}} \right) \right] \\ & + u_z \left[\frac{\partial n}{\partial z} - \frac{1}{\sqrt{1 + (y')^2 + (z')^2}} \right. \\ & \quad \left. \times \frac{d}{dx} \left(\frac{nz'}{\sqrt{1 + (y')^2 + (z')^2}} \right) \right] = 0. \end{aligned} \quad (15)$$

Since the left-hand side of Eq. (15) can only be identical to zero if all three vector components are zero, one can of course express this equation in terms of a system of three simultaneous differential equations. These three equations can, in turn, be solved with respect to y'' and z'' , which gives

and

$$z'' = \frac{1}{n} [1 + (y')^2 + (z')^2] \left(\frac{\partial n}{\partial z} - z' \frac{\partial n}{\partial x} \right). \quad (17)$$

The two last equations can be solved numerically by, for instance, using a Runge-Kutta type method or by developing a MacLaurin expansion through repeated differentiation

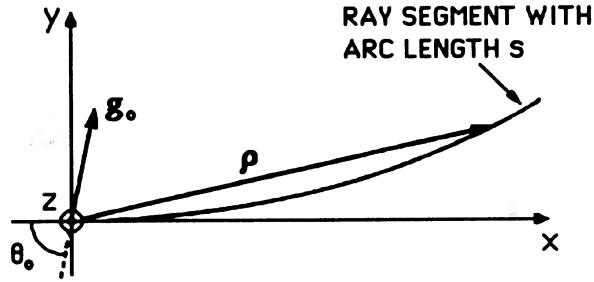


FIG. 13. Cartesian coordinate system used in defining the shape of the ray segments that make up the ray paths through the atmosphere. The origin of this system was chosen so that it coincides with the starting point of the ray segment. At the origin, the x , y , and z axes correspond to the tangent, principal normal, and binormal, respectively, of the ray segment.

of y'' and z'' with respect to x . The latter approach gives, for terms up to third order in x :

$$y(x) \approx y''(0)x^2/2 + y'''(0)x^3/6 \quad (18)$$

and

$$z(x) \approx z'''(0)x^3/6, \quad (19)$$

where

$$y''(0) = \left[\frac{1}{n} \frac{\partial n}{\partial y} \right]_0, \quad (20)$$

$$y'''(0) = \left[\frac{1}{n} \frac{\partial^2 n}{\partial x \partial y} - \frac{2}{n^2} \frac{\partial n}{\partial x} \frac{\partial n}{\partial y} \right]_0, \quad (21)$$

$$z'''(0) = \left[\frac{1}{n} \frac{\partial^2 n}{\partial x \partial z} \right]_0. \quad (22)$$

Note that the expressions enclosed in the bracket parentheses with subscripts "0" are to be evaluated at the origin of Fig. 13, i.e., at the starting point of each new ray tracing step.

The tracing of a ray through the atmosphere is performed with ray segments of varying arc lengths. It is therefore useful to have a formula relating the step size (s) and the corresponding displacement (x) along the ray tangent (cf. Fig. 13). This may be obtained by utilizing Eq. (14) to develop a MacLaurin expansion for $x(s)$. When terms up to third order in s are included, one obtains for the x coordinate of the ray segment's end point:

$$x(s) \approx s - y''(0)^2(s^3/6). \quad (23)$$

The corresponding ray deflections orthogonal to the ray tangent can now be computed from Eqs. (18) and (19), and the time $T(s)$ that it takes the photon to travel the arc length s is given by

$$T(s) \approx \frac{n_0}{c} s + \frac{1}{2c} \left[\frac{\partial n}{\partial x} \right]_0 s^2. \quad (24)$$

Before taking another step along the ray path, one also needs to determine the new ray tangent unit vector at the end point of the current ray step, $(d\mathbf{p}/ds)_s$, which may be obtained from

$$\left[\frac{d\mathbf{p}}{ds} \right]_s \approx \frac{\mathbf{u}_x + \mathbf{u}_y [y''(0)x(s) + y'''(0)x(s)^2/2] + \mathbf{u}_z z'''(0)x(s)^2/2}{\sqrt{1 + [y''(0)x(s) + y'''(0)x(s)^2/2]^2 + [z'''(0)x(s)^2/2]^2}} \quad (25)$$

When tracing rays, it is convenient to regard the atmosphere as consisting of layers bounded by sampling geoids. Between adjacent geoids, the refractivity ($n - 1$) may be treated as an exponential function of altitude. If the thickness of the layers has been chosen sufficiently small compared with the refractivity scale height, the rate of change in the refractive index with altitude (dn/dh) can be considered constant along a gravity field line connecting two adjacent sampling geoids. It should be noted, however, that the value of dn/dh may change when moving from one field line to another since the vertical distance between adjacent sampling geoids will normally be a function of latitude.

For the purpose of numerically determining the partial derivatives of n that appear in Eqs. (20)–(22), and keeping track of when a ray is passing from one layer to another, one needs the differential equations for the geoids and the gravity field lines. When expressed in terms of the geometric parameters defined in Fig. 11, the differential equation for the geoids becomes

$$dr = -r \tan \psi d\varphi. \quad (26)$$

This equation may, in turn, be used to develop a Taylor series expansion for the geoids. In the vicinity of an initial point (r_0, φ_0), one obtains

$$r = r_0 - r_0 \tan \psi_0 (\varphi - \varphi_0) - \frac{r_0}{2 \cos^3 \psi_0} \left[\frac{r_0}{R_{IM}} - \cos \psi_0 (1 + \sin^2 \psi_0) \right] (\varphi - \varphi_0)^2 + \dots \quad (27)$$

Here R_{IM} denotes the radius of curvature of the intersection between the geoid and the meridian plane at the initial point. The corresponding curvature ($1/R_{IM}$) is given by

$$\frac{1}{R_{IM}} = \frac{1}{r_0} \left(1 + \frac{1}{g_r} \left\{ \frac{\partial g_\varphi}{\partial \varphi} - \tan \psi \left[\frac{\partial g_r}{\partial \varphi} + r \left(\frac{\partial g_\varphi}{\partial r} - \tan \psi \frac{\partial g_r}{\partial r} \right) \right] \cos^2 \psi \right\} \cos \psi_0 \right), \quad (28)$$

where the expression enclosed in the parentheses with subscript "0" is to be evaluated at the point (r_0, φ_0). The partial derivatives of g_r and g_φ can be obtained by differentiating Eqs. (2) and (3) with respect to r and φ . Equation (27) can be used to step by step calculate the shape of the geoids in any latitude region where the angular velocity of the atmosphere $[\omega(r, \varphi)]$ is known.

When horizontal atmospheric variations are assumed to be negligible, the direction of the refractive index gradient is given by the gravity field lines. The differential equation for the field lines is

$$d\varphi = (1/r) \tan \psi dr, \quad (29)$$

and the altitude measured along a field line is obtained from

$$dh = dr / \cos \psi. \quad (30)$$

Equation (29) may be integrated numerically by using the following Taylor series expansion in the vicinity of an initial point (r_0, φ_0):

$$\varphi = \varphi_0 + \frac{1}{r_0} \tan \psi_0 (r - r_0) + \frac{1}{2r_0^2 \cos^3 \psi_0} \left[\frac{r_0}{R_{FL}} - \sin \psi_0 (1 + \cos^2 \psi_0) \right] (r - r_0)^2 + \dots, \quad (31)$$

where R_{FL} denotes the radius of curvature of the field line at (r_0, φ_0) . The corresponding curvature $(1/R_{FL})$ is given by

$$\frac{1}{R_{FL}} = \frac{\sin \psi_0}{r_0} \left\{ 1 + \frac{1}{g_r} \left[\frac{\partial g_\varphi}{\partial \varphi} - \tan \psi \frac{\partial g_r}{\partial \varphi} + r \left(\frac{1}{\tan \psi} \frac{\partial g_\varphi}{\partial r} - \frac{\partial g_r}{\partial r} \right) \cos^2 \psi \right] \right\}_0. \quad (32)$$

In order to find the ray solution that corresponds to a particular Doppler data sample, and in the process determine the refractive index at the ray periaxis, one needs some way of evaluating by how much each ray trial is missing the target. For this purpose, one may use the Cartesian coordinate system defined in Fig. 14 where the tracking station (P_3) lies in the $y_T z_T$ plane, the x_T axis corresponds to the incoming ray path, and the y_T axis is approximately perpendicular to the limb of the planet as viewed from the spacecraft.

The first attempt to hit the tracking station with a new ray usually results in errors both in the z_T and y_T directions. Before launching subsequent rays from the spacecraft, it is advantageous to adjust the direction of the tangent unit vector of the ray at the spacecraft, $(d\mathbf{p}/ds)_1$, so that one can eliminate the target error in the direction tangential to the limb. To first order, this amounts to rotating $(d\mathbf{p}/ds)_1$ around the spacecraft velocity vector by a small angle determined by the z_T error. This approach will essentially eliminate the z_T error in the next ray trials while at the same time keep the Doppler shift calculated from Eq. (9) equal to the observed Doppler shift. The advantage of this approach is, of course, that the y_T error in the subsequent ray trial now is basically a function only of the vertical refractive index gradient chosen near the ray periaxis.

Next, two new ray trials are launched from the spacecraft in the direction obtained in the manner indicated above but by using different refractive index gradients near the ray periaxis. These two gradients together with the corresponding y_T errors are then employed in an interpolation scheme to calculate the refractive index gradient to eliminate

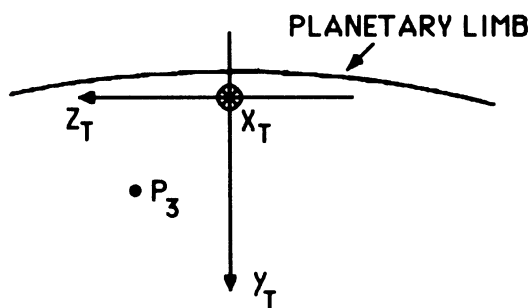


FIG. 14. Target coordinate system as viewed from the spacecraft. The x_T axis corresponds to the incoming ray path and the tracking station (P_3) lies in the $y_T z_T$ plane which we shall also refer to as the target plane. The y_T axis is parallel to the projection into the target plane of the principal ray normal at the ray periaxis.

the error in the y_T direction, and thus make the photon hit the tracking station. If necessary, the procedure is repeated until the y_T and z_T errors are within acceptable limits. The accuracy of the numerical integration may be monitored by tracing the ray from the station and back to the spacecraft. The final solution allows the refractive index of the atmosphere to be determined at the periaxis of the sampling ray, i.e., at the point where the ray tangent is perpendicular to the local vertical and the ray touches the sampling geoid.

When the refractive index has been computed, one can proceed to determine the absorption coefficient of the atmosphere. In order to do this, one must first calculate the defocusing expected for each sampling ray. The defocusing may be obtained by tracing a set of auxiliary rays which start at the same point (P_1) as the sampling ray but take off in slightly different directions and therefore are refracted towards the Earth via different paths. Together with the sampling ray, these auxiliary rays form a thin ray pencil or tube where the radiant energy is traveling from the spacecraft to the Earth. By comparing the flux density of the radiation reaching the tracking station via this ray tube through the atmosphere with the flux density at the station before the link entered the atmosphere, one can determine the decrease in the recorded signal intensity that was caused by refractive defocusing. The effect of defocusing must, of course, be removed from the signal intensity perturbations recorded at the tracking station before the absorption loss can be determined for each sampling ray. When this has been done, the "residual absorption loss" suffered by the sampling ray in the lowest layer it reached is computed by subtracting the loss suffered while passing through higher layers from the total absorption loss along the ray. Finally, one obtains an estimate of the absorption per unit of path length in the lowest layer reached by the sampling ray by dividing the residual absorption loss with the arc length of the ray within the lowest layer.

Under otherwise equal conditions, one obtains the most reliable occultation profiles when the spacecraft is setting or rising approximately perpendicular to the limb of the planet as viewed from the Earth. This experiment configuration is of considerable practical interest because it reduces the size of the region probed by the link and therefore the errors that horizontal refractivity and absorptivity variations can produce in the vertical profiles inferred from the measurements. Another advantage with this type of occultation geometry is that the latitude interval covered by the measurements usually is small enough so that variations in the atmospheric rotation period determined from the cloud motion may be neglected, and this allows the acceleration of gravity (g) to be expressed in terms of the gradient of a potential function in the region probed by the tracking link. Thus in this case, one has

$$g = \text{grad}[U(r, \varphi)], \quad (33)$$

where $U(r, \varphi)$ is obtained by integrating Eqs. (2) and (3) with respect to r and φ . This gives

$$U(r, \varphi) = \frac{GM}{r} \left[1 - \sum_{i=1}^{\infty} J_{2i} \left(\frac{R_j}{r} \right)^{2i} P_{2i}(\sin \varphi) \right] + \frac{1}{3} \omega^2 r^2 [1 - P_2(\sin \varphi)]. \quad (34)$$

When defined in this manner, $U(r, \varphi)$ has a constant positive value along each geoid and is increasing with increasing

depth. As indicated above, Eq. (34) is applicable in atmospheric regions where ω is constant² and independent of r and φ .

It should be noted here that the geoid potential function, $U(r, \varphi)$, differs in several respects from the Newtonian gravity potential, U_N , which is used in the calculation of the gravitational frequency shift expected from the general theory of relativity [cf. Eq. (9)]. For example, $U(r, \varphi)$ and U_N have opposite signs in front of terms containing GM/r . Furthermore, $U(r, \varphi)$ is a function of the angular velocity of the atmosphere (ω) but does not depend on the masses of the sun and the Earth—while the opposite is true with regard to U_N .

The use of $U(r, \varphi)$ simplifies the ray tracing calculations because (1) it provides a more convenient measure of the level to which the ray has penetrated the atmosphere than the depth measured along gravitational field lines, and (2) it allows the refractive index to be treated as a function of a single variable. In what follows, we shall first discuss the case where the thickness of the atmospheric layers has been chosen small enough compared with the refractivity scale height so that one can treat the refractivity as a piecewise linear function of U . Later, we come back to the more general problem where the refractivity is considered a piecewise exponential function of the potential.

In the piecewise linear case, dn/dU is constant within each layer. Thus, at a point with potential $U_j + \Delta U$ that is located between sampling geoids with potentials U_j and U_{j+1} (where $U_{j+1} > U_j$), the refractive index, $n(U_j + \Delta U)$, is given by

$$n(U_j + \Delta U) = n(U_j) + \frac{dn}{dU} \Delta U, \quad (35)$$

where

$$\frac{dn}{dU} = \frac{n(U_{j+1}) - n(U_j)}{U_{j+1} - U_j}. \quad (36)$$

With these simplifying assumptions, one can relate the spatial distribution of n more explicitly to the properties of the gravity field. For the partial derivatives that appear in Eqs. (20)–(22), one can now show that

$$\left[\frac{\partial n}{\partial x} \right]_0 = \frac{dn}{dU} g_0 \cos \theta_0, \quad (37)$$

$$\left[\frac{\partial n}{\partial y} \right]_0 = \frac{dn}{dU} g_0 \sin \theta_0, \quad (38)$$

$$\left[\frac{\partial^2 n}{\partial x \partial y} \right]_0 = \frac{dn}{dU} \left[\frac{1}{2} \left(\frac{g}{R_{IO}} - \frac{\partial g}{\partial h} \right) \sin 2\theta - \frac{\partial g}{\partial L} \cos 2\theta \cos \gamma \right]_0 \quad (39)$$

²In general, one can show that g can be expressed as the gradient of a potential function when $\omega(r, \varphi)$ satisfies the differential equation:

$$\frac{1}{r} \frac{\partial \omega}{\partial \varphi} = - \frac{\partial \omega}{\partial r} \tan \varphi.$$

This equation has a general solution of the form $\Omega(r \cos \varphi)$ which implies that ω must be a function only of the distance to the spin axis of the planet. In other words, the angular velocity of the atmosphere must be constant on cylinders whose axes coincide with the spin axis. However, this circulation model does not appear to have any practical applications in the study of radio occultation data because none of the planets in our solar system have atmospheres that behave in this manner.

$$\left[\frac{\partial^2 n}{\partial x \partial z} \right]_0 = - \frac{dn}{dU} \left[g \left(\frac{1}{R_{IM}} - \frac{1}{R_{PM}} \right) \sin \theta \cos \gamma - \frac{\partial g}{\partial L} \cos \theta \right]_0 \sin \gamma_0. \quad (40)$$

As indicated by the bracket parentheses with subscripts “0,” the parameters that appear in these equations are to be determined at the beginning of each ray step; i.e., at the origin of the coordinate system shown in Fig. 13. Since the value of dn/dU changes at the sampling geoids which serve as layer boundaries, one achieves the best ray tracing accuracy when no ray segment is allowed to cross from one layer and into the next. When a ray segment reaches a sampling geoid, it should therefore be terminated and a new ray segment started.

Among the new symbols used here, θ_0 is the angle between the x axis and g_0 (cf. Fig. 13), and g is the magnitude of the acceleration of gravity:

$$g = \sqrt{g_r^2 + g_\varphi^2}. \quad (41)$$

Furthermore, R_{IO} is the radius of curvature of the intersection between the xy plane (or osculating plane) and the local geoid at the origin. The corresponding curvature ($1/R_{IO}$) is given by

$$\frac{1}{R_{IO}} = \frac{\cos^2 \gamma_0}{R_{IM}} + \frac{\sin^2 \gamma_0}{R_{PM}}. \quad (42)$$

Here, γ_0 is the azimuth angle of the x axis as measured from the direction of local north towards the east, and R_{IM} and R_{PM} are the radii of curvature of the local geoid in the meridian plane and perpendicular to the meridian plane, respectively. The corresponding curvatures are given by Eqs. (43) and (44)

$$\frac{1}{R_{IM}} = \frac{1}{r_0} \left\{ 1 + \frac{1}{g_r} \left[\frac{\partial g_\varphi}{\partial \varphi} + r \tan \psi \left(\tan \psi \frac{\partial g_r}{\partial r} - 2 \frac{\partial g_\varphi}{\partial r} \right) \right] \right\} \cos^3 \psi_0, \quad (43)$$

$$\frac{1}{R_{PM}} = \frac{\cos(\varphi_0 + \psi_0)}{r_0 \cos \varphi_0}. \quad (44)$$

Note that Eq. (43) is applicable only to regions where ω is constant and independent of r and φ .

Finally, the partial derivatives of g with respect to h and L are

$$\frac{\partial g}{\partial h} = - \left\{ \frac{\partial g_r}{\partial r} + \tan \psi \left[\frac{\partial g_\varphi}{\partial r} + \frac{1}{r} \left(\frac{\partial g_r}{\partial \varphi} + \tan \psi \frac{\partial g_\varphi}{\partial \varphi} \right) \right] \right\} \cos^2 \psi, \quad (45)$$

$$\frac{\partial g}{\partial L} = \left[- \frac{1}{r} \left(\frac{\partial g_r}{\partial \varphi} + \tan \psi \frac{\partial g_\varphi}{\partial \varphi} \right) + \tan \psi \left(\frac{\partial g_r}{\partial r} + \tan \psi \frac{\partial g_\varphi}{\partial r} \right) \right] \cos^2 \psi, \quad (46)$$

where h is the altitude measured along the local gravity field line and L is the distance measured towards the north along the intersection between the local geoid and meridian plane. The partial derivatives of g_r and g_φ with respect to r and φ may be obtained by differentiating Eqs. (2) and (3) while treating ω as a constant.

Note that when the ray solution for a new Doppler data sample is to be obtained, the value of dn/dU is known in all the higher layers probed by preceding sampling rays. Thus, it is only in the region below the sampling geoid touched by the previous ray that dn/dU must be determined. Together with the potential at the periapsis of the new sampling ray, the value of dn/dU in the new layer allows the refractive index to be computed at the new sampling geoid.

In some cases, one may find that the ray being traced fails to penetrate the sampling geoid touched by the preceding ray and therefore has a sampling geoid (j) that is located above the sampling geoid of the preceding ray ($j-1$). In other words, U_j is less than U_{j-1} . This means that the data have not been sorted according to decreasing ray periapsis altitudes and that the preceding ray must be retraced.

When a piecewise exponential refractive index model is used in the inversion process, the refractive index

$n(U_j + \Delta U)$ at a point between two adjacent geoids with potentials U_j and U_{j+1} (where $U_{j+1} > U_j$) is given by

$$n(U_j + \Delta U) = 1 + [n(U_j) - 1]e^{K\Delta U}, \quad (47)$$

where

$$K = \frac{\ln([n(U_{j+1}) - 1]/[n(U_j) - 1])}{U_{j+1} - U_j}. \quad (48)$$

This formulation leads to slightly modified expressions for the partial derivatives of n with respect to x , y , and z . The new expressions can be obtained by replacing dn/dU with $(n_0 - 1)K$ in Eqs. (37), (38), (39), and (40). In addition, one must add the term $\frac{1}{2}(n_0 - 1)K^2 g_0^2 \sin(2\theta_0)$ to the expression on the right-hand side of Eq. (39). Except for the fact that one, in the piecewise exponential case, must solve for K instead of dn/dU in each layer, the basic inversion procedure is the same as for the piecewise linear case.

REFERENCES

- Allison, M. D. 1982, Ph.D. thesis, Rice University, Houston, Texas
 Allison, M. D. 1990, *Icarus*, 83, 282
 Anderson, J. D., Campbell, J. K., Jacobson, R. A., Sweetnam, D. N., Taylor, A. H., Prentice, A. J. R., & Tyler, G. L. 1987, *J. Geophys. Res.*, 92, 14877
 Appleby, J. F. 1986, *Icarus*, 65, 383
 Baines, K. H., & Smith, W. H. 1990, *Icarus*, 85, 65
 Berge, G. L., & Gulkis, S. 1976, in *Jupiter*, edited by T. Gehrels (University of Arizona, Tucson)
 Bézard, B., 1983, *Icarus*, 55, 259
 Boggs, J. E., Crain, C. M., & Whiteford, J. E. 1957, *J. Phys. Chem.*, 61, 482
 Bose, T. K., Sochanski, J. S., & Cole, R. H. 1972, *J. Chem. Phys.*, 57, 3592
 Broadfoot, A. L., 1989, *Sci*, 246, 1459
 Campbell, J. K., & Synnott, S. P. 1985, *AJ*, 90, 364
 Campbell, J. K., & Anderson, J. D. 1989, *AJ*, 97, 1485
 Conrath, B., 1989, *Sci*, 246, 1454
 Conrath, B. J., Gautier, D., Lindal, G. F., Samuelson, R. E., & Shaffer, W. A. 1991, *J. Geophys. Res.* (in press)
 Davies, M. E., 1986, *Celest. Mech.*, 39, 103
 de Pater, I., & Richmond, M. 1989, *Icarus*, 80, 1
 de Pater, I., Romani, P. N., & Atreya, S. K. 1991, *Icarus*, 91, 220
 Edelson, R. E., Madsen, B. D., Davis, E. K., & Garrison, G. W. 1979, *Sci*, 204, 913
 Eshleman, V. R. 1973, *Planet Space Sci.*, 21, 1521
 Eshleman, V. R., Tyler, G. L., Anderson, J. D., Fjeldbo, G., Levy, G. S., Wood, G. E., & Croft, T. A. 1977, *SSRv*, 21, 207
 Eshleman, V. R., Hinson, D. P., Lindal, G. F., & Tyler, G. L. 1987, *Adv. Space Res.*, 7 (12), 29
 Essen, L. 1953, *Proc. Phys. Soc. London, Sec. B*, 66, 189
 Fegley, B., Gautier, D., Owen, T., & Prinn, R. G. 1991, in *Uranus*, edited by J. T. Bergstrahl, E. D. Miner, and M. S. Matthews (University of Arizona, Tucson)
 Fink, U., & Larson, H. P. 1979, *ApJ*, 233, 1021
 Fjeldbo, G., & Eshleman, V. R. 1968, *Planet Space Sci.*, 16, 1035
 Fjeldbo, G., Kliore, A. J., & Eshleman, V. R. 1971, *AJ*, 76, 123
 Flasar, F. M., Conrath, B. J., Gierasch, P. J., & Pirraglia, J. A. 1987, *J. Geophys. Res.*, 92, 15011
 French, R. G., Elliot, J. L., & Levine, S. E. 1986, *Icarus*, 67, 134
 Gennaoui, A. 1951, *Helvetica Physica Acta*, 24, 401
 Gierasch, P. J., & Conrath, B. J. 1987, *J. Geophys. Res.*, 92, 15019
 Ham, N. C., Rebold, T. A., & Weese, J. F. 1989, TDA Progress Report No. 42-97 (Jet Propulsion Laboratory, Pasadena, CA), p. 252
 Hammel, H. B., Beebe, R. F., De Jong, E. M., Hansen, C. J., Howell, C. D., Ingersoll, A. P., Johnson, T. V., Limaye, S. S., Magalhaes, J. A., Pollack, J. B., Sromovsky, L. A., Suomi, V. E., & Swift, C. E. 1989, *Sci*, 245, 1367
 Hinson, D. P., & Tyler, G. L. 1983, *Icarus*, 54, 337
 Hinson, D. P. 1986, *Radio Sci.*, 21, 257
 Hinson, D. P., & Eshleman, V. R. 1988, *BAAS*, 20, 822
 Houghton, J. T. 1977, *The Physics of Atmospheres* (Cambridge University Press, Cambridge), p. 19
 Hubbard, W. B., 1987, *Icarus*, 72, 635
 Joiner, J., & Steffes, P. G. 1991, *J. Geophys. Res.*, 96, 17470
 Kursinski, E. R., & Asmar, S. W. 1991, TDA Progress Report No. 42-105 (Jet Propulsion Laboratory, Pasadena, CA), p. 109
 Larson, H. P., Davis, D. S., Hofmann, R., & Bjoraker, G. L. 1984, *Icarus*, 60, 621
 Lindal, G. F., Sweetnam, D. N., & Eshleman, V. R., 1985, *AJ*, 90, 1136
 Lindal, G. F., Lyons, J. R., Sweetnam, D. N., Eshleman, V. R., Hinson, D. P., & Tyler, G. L. 1987, *J. Geophys. Res.*, 92, 14987
 Lindal, G. F., Lyons, J. R., Sweetnam, D. N., Eshleman, V. R., Hinson, D. P., & Tyler, G. L. 1990, *Geophys. Res. Lett.*, 17, 1733
 Maryott, A. A., & Buckley, F. 1953, National Bureau of Standards Circular 537 (U.S. Government Printing Office, Washington, DC)
 Massie, S. T., & Hunten, D. M. 1982, *Icarus*, 49, 213
 Nelson, R. D., Lide, D. R., & Maryott, A. A. 1967, National Standard Reference Data Series—National Bureau of Standards 10 (U.S. Government Printing Office, Washington, DC)
 Orcott, R. H., & Cole, R. H. 1967, *J. Chem. Phys.*, 46, 697
 Orton, G. S., Griffin, M. J., Ade, P. A. R., Nolt, I. G., Radostitz, J. V., Robson, E. I., & Gear, W. K. 1986, *Icarus*, 67, 289
 Owen, T., McKellar, A. R. W., Encrenaz, T., Lecacheux, J., de Bergh, C., & Maillard, J. P. 1977, *A&A*, 54, 291
 Poynter, R. L., & Pickett, H. M. 1981, JPL Publication 80-23 (Jet Propulsion Laboratory, Pasadena, CA)
 Prinn, R. G., Larson, H. P., Caldwell, J. J., & Gautier, D. 1984, in *Saturn*, edited by T. Gehrels and M. S. Matthews (University of Arizona, Tucson), p. 88
 Rages, K. A., & Pollack, J. B. 1989, Paper presented at the annual DPS meeting, American Astronomical Society, Providence, Rhode Island, October 31–November 3
 Reid, R. C., Prausnitz, J. M., & Poling, B. E. 1987, *The Properties of Gases and Liquids* (McGraw-Hill, New York)
 Romani, P. N., de Pater, I., & Atreya, S. K. 1989, *Geophys. Res. Lett.*, 16, 933
 Smith, B. A., 1989, *Sci*, 246, 1422
 Spilker, T. R. 1990, Ph.D. thesis, Stanford University, Stanford, CA
 Stone, E. C., & Miner, E. D. 1989, *Sci*, 246, 1417
 Townes, C. H., & Schawlow, A. L. 1955, *Microwave Spectroscopy* (McGraw-Hill, New York)
 Tyler, G. L., 1986, *Sci*, 233, 79
 Tyler, G. L., 1989, *Sci*, 246, 1466
 Warwick, J. W., 1986, *Sci*, 233, 102
 Warwick, J. W., 1989, *Sci*, 246, 1498